

---

# Center-based 3D Object Detection and Tracking

---

Tianwei Yin

UT Austin

yintianwei@utexas.edu

Xingyi Zhou

UT Austin

zhouxy@cs.utexas.edu

Philipp Krähenbühl

UT Austin

philkr@cs.utexas.edu

## Abstract

Three-dimensional objects are commonly represented as 3D boxes in a point-cloud. This representation mimics the well-studied image-based 2D bounding-box detection, but comes with additional challenges. Objects in a 3D world do not follow any particular orientation, and box-based detectors have difficulties enumerating all orientations or fitting an axis-aligned bounding box to rotated objects. In this paper, we instead propose to represent, detect, and track 3D objects as points. We use a keypoint detector to find centers of objects, and simply regress to other attributes, including 3D size, 3D orientation, and velocity. In our center-based framework, 3D object tracking simplifies to greedy closest-point matching. The resulting detection and tracking algorithm is simple, efficient, and effective. On the nuScenes dataset, our point-based representations perform 3-4 mAP higher than the box-based counterparts for 3D detection, and 6 AMOTA higher for 3D tracking. Our real-time model runs end-to-end 3D detection and tracking at 30 FPS with 54.2 AMOTA and 48.3 mAP while the best single model achieves 60.3 mAP for 3D detection, and 63.8 AMOTA for 3D tracking. The code and pretrained models are available at <https://github.com/tianweiy/CenterPoint>.

## 1 Introduction

Strong 3D perception is a core ingredient in many state-of-the-art driving systems [1, 30]. Compared to the well-studied 2D detection problem, 3D detection from point-clouds offers a series of interesting challenges: First, point clouds are sparse, and most regions of 3D space are without measurements [16]. Second, the resulting output is a three-dimensional box, that is often not well aligned with any global coordinate frame. Third, 3D objects come in a wide range of sizes, shapes, and aspect ratios, e.g., in the traffic domain, bicycles are near planar, buses and limousines elongated, and pedestrians tall. These marked differences between 2D and 3D detection, made a transfer of ideas between the two domain harder [27, 28, 39]. The crux of it is that an axis-aligned 2D box [10, 11] is a poor proxy of a free-form 3D object. One solution might be to classify a separate template (anchor) for each object orientation [37, 38], but this unnecessarily increases the computational burden, and introduces a large number of potential false-positive detections. We argue that the main underlying challenge in linking up the 2D and 3D domains lies in this representation of objects.

In this paper, we show how representing objects as points greatly simplifies 3D recognition to a degree at which we can apply a center-based 2D detector [42] to 3D detection without major modifications, except for the backbone architecture. Specifically, our detector uses a standard Lidar-based backbone network, like VoxelNet [44] or PointPillars [18] to build a representation of the input point cloud. We then flatten features from this representation into an overhead map-view, and use a standard image-based keypoint detector to find object centers. For each detected center, we regress to all other object properties such as 3D size, orientation, and velocity.

The center-based representation has several key advantages: First, unlike bounding boxes, points have no intrinsic orientation. This greatly reduces the search space of the object detector, while allowing the backbone to learn the rotational invariance of objects, and rotational equivariance of their relative

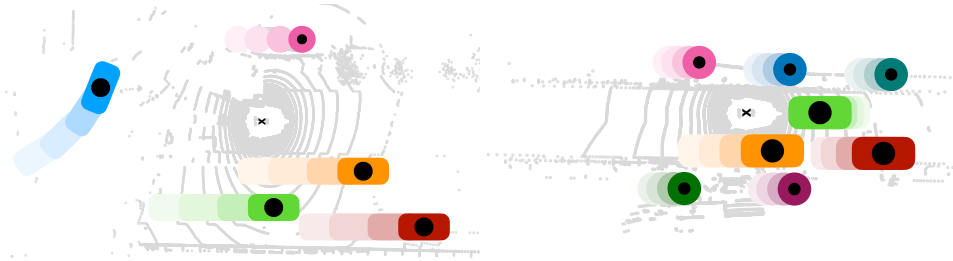


Figure 1: We represent, detect, and track 3D objects as points. All other attributes are regressed from the center feature. Objects are tracked by estimating the motion of their center between consecutive frames. Best viewed in color.

rotation. Second, a center-based representation simplifies downstream tasks such as tracking. If objects are points, tracklets are paths in space and time. Our tracker follows CenterTrack [41] and simply predicts the relative offset (velocity) of objects between consecutive frames. These frames are then linked up greedily. Third, in 3D detection, object localization matters more than full-fledged 3D estimation of all 3D properties of a detected object. This is reflected in common evaluation metrics [4] that primarily rely on the distance between the centers of detected objects instead of properties of the estimated 3D box. Our detector primarily focuses on this localization, and separately estimates other object properties.

We evaluate our 3D recognition system on nuScenes detection and tracking benchmarks. We show that a simple switch of representation from the standard box-based detection to center-based detection yields a 3-4 mAP increase in detection performance and a 6 AMOTA increase in tracking performance across different backbone architectures [18, 35, 44, 45]. In the real-time regime (30 FPS), our model achieves 48.3 mAP, comparable to the best prior offline methods. Using a heavier backbone with sparse-convolutional layers, the model achieves a 60.3 mAP, outperforming the prior state-of-the-art ensemble by 7.5 mAP. For 3D tracking, our model performs at 63.8 AMOTA outperforming the prior state-of-the-art by 8.8 AMOTA. These experimental results highlight the merits of point-based representations for 3D recognition.

## 2 Related work

**2D object detection** predicts axis-aligned bounding box from image input. The RCNN family [10, 11, 15, 26] finds a category-agnostic bounding box candidates (anchor), then classify and refine it. YOLO [25], SSD [21], and RetinaNet [20] directly find a category-specific box candidate, sidestepping later classification and refinement. Center-based detectors, e.g. CenterNet [42] or CenterTrack [41], directly detect the implicit object center point without the need for candidate boxes. Many 3D object detectors [27, 28, 39] evolved from these 2D object detector. We argue center-based representation [41, 42] is a better fit in 3D application comparing to axis-aligned boxes.

**3D object detection** aims to predict three dimensional rotated bounding boxes. Vote3Deep [8] leverages feature-centric voting [31] to implement sparse convolution for efficient 3D point cloud processing on equally spaced 3D voxels [31]. VoxelNet [44] uses a PointNet [24] inside each voxel to generate a unified feature representation. The combined features are passed into a Region Proposal Network(RPN) with 3D sparse convolutions [12] and 2D convolutions to generate detections. SECOND [35] speeds up VoxelNet by using a simplified voxel encoder and fast sparse 3D convolutions. And SA-SSD [14] further improves SECOND by adding two auxiliary point-level tasks to learn structure-aware features. To remove the expensive 3D convolutions, PIXOR [36] project all points onto a 2D feature map with 3d occupancy and point intensity information encoded in the feature dimension. PointPillars [18] replaces all voxel computation with a pillar representation, a single tall elongated voxel per map location, improving backbone efficiency. MVF [43] combines multiple view features to learn a more effective pillar representation. PointPainting [29] incorporate a 3D semantic segmentation into the point-cloud. Hu et al. [16] additionally reason about free space and visibility. Our framework is compatible with both voxel and pillar-based backbones, and improves both. Recently, VoteNet [23] detects objects through vote clustering using point feature sampling and grouping. In contrast, we directly regress to 3D bounding boxes through features at the center point without voting. Wong et al. [34] and Chen et al. [5] used similar multiple points representation in the object center region (i.e., point-anchors) and regress to other attributes, while we use a single positive cell for each object and use a keypoint estimation loss.

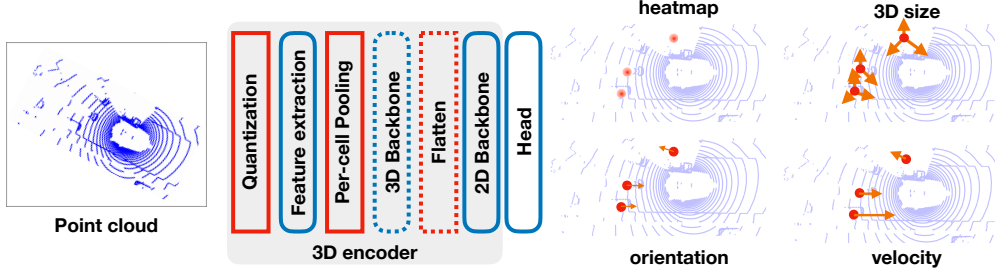


Figure 2: Overview of our detection framework. We rely on a standard 3D encoding architecture that quantizes Lidar points into cells, extracts point features, pools over cells, optionally applies a 3D CNN before flattening the representation into a 2D map view. Finally, a 2D CNN architecture and detection head produces four outputs: A heatmap indicating object centers, 3D size, orientation, and velocity estimates for each center. We show deep networks in blue and fixed operations in red.

**3D object tracking.** Many 2D tracking algorithms [2, 3, 17, 33] readily track 3D objects out of the box. However, dedicated 3D trackers based on 3D Kalman filters [6, 32] still have an edge as they better exploit the three-dimensional motion in a scene. Here, we adopt a much simpler approach following CenterTrack [41]. We show that the velocity estimate, together with the point-based detection is sufficient to track centers of objects through multiple frames. This tracker is much faster, and more accurate than dedicated 3D trackers [6, 32].

### 3 Preliminary

Let  $\mathcal{P} = \{(x, y, z, r)_i\}$  be an orderless point cloud of 3D location  $(x, y, z)$  and reflectance  $r$  measurements. 3D object detection aims to predict a set of 3D object bounding boxes  $\mathcal{B} = \{b_k\}$  in the bird eye view from this point-cloud. Each bounding box  $b = (u, v, d, w, l, h, \alpha)$  consists of a center location  $(u, v, d)$ , relative to the objects ground plane, and 3D size  $(w, l, h)$ , and rotation expressed by yaw  $\alpha$ . Without loss of generality, we use an egocentric coordinate system. The sensor is at coordinate  $(0, 0, 0)$  at a yaw  $\alpha = 0$ .

Instead of directly predicting output on the irregular point cloud  $\mathcal{P}$ , most modern 3D object detectors [14, 18, 35, 44] use a series of intermediate representations, as shown in Figure 2. A 3D encoder first quantizes the point cloud into regular bins. A point-based network [24] then extracts features for all points inside a bin. The 3D encoder then pools these features into its primary feature representation. Most of the computation happens in the backbone network, which operates solely on these quantized and pooled feature representations. Finally, the quantized output representation is flattened into a planar map-view, and passed through a 2D convolutional backbone. The output of the 3D encoder is a feature-map  $\mathbf{M} \in \mathbb{R}^{W \times L \times F}$  of width  $W$  and length  $L$  with  $F$  channels in a map-view reference frame. A detection head, most commonly a one- [20] or two-stage [26] bounding-box detector, then produces object detections from this overhead feature-map. In this paper, we introduce a novel center-based head design, but rely on off-the-shelf 3D encoders, namely VoxelNet [35, 44] and PointPillars [18].

**VoxelNet** quantizes unordered Lidar points into small 3D voxels using a process called Voxelization. Points outside the quantization range are discarded. A PointNet [24] then extracts 3D features within each voxel, and per-voxel max- or average-pooling then converts the point features into a fixed size representation. The resulting 3D feature map serves as an input to a 3D convolutional backbone network (usually implemented with sparse convolution [12, 35]). Striding in the backbone trades the spatial output resolution for computational efficiency. Finally, all voxels along the height dimension are collapsed into a map-view representation and processed by a 2D CNN to produce the feature-map  $\mathbf{M}$ . We follow SECOND [35] and adopt a simplified version of the voxel feature extractor, which simply takes the average of point-wise features inside a voxel.

**PointPillars** collapse the height dimension in the beginning and quantize into a tall voxel representation, called Pillars, along a regular 2D grid. Each map-view location corresponds to exactly one Pillar. PointPillars use a hand-designed 9-dimensional feature extractor that includes 3D location (3), intensity (1), offsets to 3D pillar center (3), and offsets to 2D grid center (2), followed by a

single linear transformation and per-pillar max-pooling into a fixed-size representation. The pillar representation is inherently 2D, thus skips the 3D backbone and consecutive flattening. However, PointPillars still use a 2D CNN to produce the output feature-map  $\mathbf{M}$ . In general, a Pillar-based backbone is faster, but slightly less accurate.

**2D CenterNet.** CenterNet [42] rephrases object detection as keypoint estimation. It takes an input image and predicts a  $w \times h$  heatmap  $\hat{Y} \in [0, 1]^{w \times h \times K}$  for each of  $K$  classes. Each local maximum (i.e., pixels whose value is greater than its 8 neighbors) in the output heatmap corresponds to the center of a detected object. To retrieve a 2D box, CenterNet regresses to a size map  $\hat{S} \in \mathbb{R}^{w \times h \times 2}$  shared between all categories. For each detection object, the size-map stores its width and height at the center location. The CenterNet architecture uses a standard fully convolutional image backbone, and adds a dense prediction head on top. During training, CenterNet learns to predict heatmaps with rendered Gaussian kernels at each annotated object center  $\mathbf{q}_i$  for each class  $c_i \in \{1 \dots K\}$ . Specifically, for each pixel  $\mathbf{p}$  the target heatmap is  $Y_{\mathbf{p},k} = \max_{i:c_i=k} \exp(-\frac{(\mathbf{p}-\mathbf{q}_i)^2}{2\sigma_i^2})$ , where  $\sigma_i$  changes depending on the size of the object. Training uses the focal loss [20]:

$$L_{hm} = -\frac{1}{N} \sum_{\mathbf{p},k} \begin{cases} (1 - \hat{Y}_{\mathbf{p},k})^\alpha \log(\hat{Y}_{\mathbf{p},k}) & \text{if } Y_{\mathbf{p},k} = 1 \\ (1 - Y_{\mathbf{p},k})^\beta (\hat{Y}_{\mathbf{p},k})^\alpha \log(1 - \hat{Y}_{\mathbf{p},k}) & \text{otherwise} \end{cases} \quad (1)$$

where  $\alpha = 2$  and  $\beta = 4$  are hyper-parameters and  $N$  is the number of objects. The size prediction  $\hat{S}$  is supervised only at the ground truth peak locations using an L1 loss:

$$L_{size} = \frac{1}{N} \sum_{i=1}^N |\hat{S}_{\mathbf{q}_i} - \mathbf{s}_i| \quad (2)$$

where  $\mathbf{s}_i$  is the annotated 2D bounding box size of the  $i$ -th object.

To make up for quantization errors introduced by the striding of the backbone architecture, CenterNet also regresses to a local offset  $\hat{O}$ , trained with  $L_{local} = \frac{1}{N} \sum_{i=1}^N |\hat{O}_{\mathbf{q}_i} - (\mathbf{q}_i - [\mathbf{q}_i])|$ . The overall training objective is a weighted combination of the heatmap focal loss, size, and local offset:

$$L = L_{hm} + \lambda_{size} L_{size} + \lambda_{local} L_{local} \quad (3)$$

where the  $\lambda$ s are the loss weights.

At test time, the detector produces  $K$  heatmaps, and dense class-agnostic regression maps. Each local maxima (peak) in the heatmaps corresponds to an object, with confidence proportional to the heatmap value at the peak. For each detected object, the detector retrieves all regression values from the regression maps at the corresponding peak location. Depending on the application domain, Non-Maxima Suppression (NMS) may be warranted.

In the next section, we show how to adapt this center-based architecture to 3D detection.

## 4 CenterPoint

We now design a center-based detection head for 3D Lidar based detection. Our head design follows the 2D image-based CenterNet. Specifically, let  $\mathbf{M} \in \mathbb{R}^{W \times H \times F}$  be the output of the 2D backbone. Our head uses three  $3 \times 3$ -convolutional layers separated by a rectified linear unit and batch-norm. The last convolutional layer produces all required outputs for our detector: A  $K$ -channel heatmap  $\hat{Y}$  indicating object centers for  $K$  classes, a dense object size prediction  $\mathbf{s} = (w, l, h)$ , a three-dimensional local offset  $\mathbf{o} = (o_x, o_y, o_z)$ , and rotation estimate  $\mathbf{e} = (\sin(\alpha), \cos(\alpha))$ . These outputs follow the standard training procedure of CenterNet described in the previous section: A focal loss Equation (1) to supervise the heatmap  $\hat{Y}$ , L1 regression for orientation and local offset, and log-space L1 regression [5] for size  $\frac{1}{N} \sum_{i=1}^N |\hat{S}_{\mathbf{q}_i} - \log(\mathbf{s}_i)|$ . The center-based representation has one key advantage during training: It anchors an object at its 3D center, without first having to estimate a 2D bounding box. This allows for the seamless transition for a 2D head design to our 3D detector. While the main idea and architecture of our framework are straightforward, there are a few subtle differences between the 2D and 3D domains.

## 4.1 Making it work

**Target Heatmap  $Y$ .** Objects in a top-down map view are sparser than in an image. In map-view distances are absolute, while an image-view distorts them by perspective. Consider a road scene, in map-view the area occupied by vehicles small, but in image-view, a few large objects may occupy most of the screen. Furthermore, the compression of the depth-dimension in perspective projection naturally places object centers much closer to each other in image-view. Following, the standard supervision of CenterNet results in a very sparse supervisory signal, where most locations are considered background. To counteract this, we increase the positive supervision for the target heatmap  $Y$  by enlarging the Gaussian peak rendered at each ground truth object center. Specifically, we set the Gaussian radius to  $\sigma = \max(f(wl, r), \tau)$ , where  $\tau$  is the smallest allowable Gaussian radius, and  $f$  is the radius function defined in CornerNet [19] that negatively correlates to  $r$ . I.e. smaller  $r$  corresponds to larger radius. We use  $\tau = 2$  and  $r = 0.1$ .

**Detection head.** 3D bounding boxes are not axis-aligned in the bird-eye view. This means that an efficient backbone architecture needs to learn rotational invariance and equivariance. To help the network better capture rotational properties, we add one layer of deformable convolution [7]. Specifically, we separate the head into center prediction  $Y$  branch and regression branch. Both branches share the first convolution, but then use a separate deformable convolution layer: Center prediction to capture rotational invariance, regression to capture rotational equivariance. Both branches produce all their outputs using two final  $3 \times 3$  convolutions.

**Circular NMS.** We follow Zhou *et al.* [42] and replace the standard non-maxima suppression (NMS) with a fast max-pooling based NMS. However, since the overhead map-view is rotationally invariant, we chose circular pooling region, instead of square box. Specifically, an object is only counted as positive if no other center with a higher confidence exists within a radius  $r$  using a bird-eye view distance metric. Circular NMS works as well as 3D-IoU-based metrics, but is much faster.

**Double-flip testing.** The resulting detector is still not perfectly rotationally invariant or equivariant. We can exploit this, and build a simple ensemble of four rotated copies of the input point cloud. Specifically, we pass the input point-cloud through CenterPoint using all four combinations of horizontal and vertical flipping. Each produces a heatmap  $\hat{Y}$  and regression targets. We simply average these outputs to produce an ensembled output: For heatmaps first apply a sigmoid transform, for all regression outputs we undo the coordinate transform. This simple averaging is only possible in a center-based representation, and would not directly work for box-based detectors.

**Velocity prediction and tracking** To track objects through time, we learn to predict a velocity estimate  $\mathbf{v}$  for each detected object as an additional regression output. The velocity estimate predicts the difference in object position between the current and the past frame, similar to CenterTrack [41].

We use this offset to associate current detections to past ones in a greedy fashion. Specifically, we project the object centers in the current frame back to the previous frame by applying the negative velocity estimate, then match them to the tracked objects by closest distance matching. Following SORT [3], we keep unmatched tracks up to  $T = 3$  frames before deleting them. We update each unmatched track with its last known velocity estimation. See supplement for details.

## 5 Experiments

We evaluate both 3D detection and 3D tracking on the recently published large scale nuScenes dataset [4]. nuScenes contains 1000 driving sequences, with 700, 150, 150 sequences for train, validation, and testing, respectively. Each sequence is approximately 20-second long, with Lidar frequency 20 FPS. The dataset provides calibrated vehicle pose information for each Lidar frame, but only provides box annotations every 10 frames (0.5s). In total, there are 28k, 6k, 6k, annotated frames for training, validation, and testing, respectively.

A common practice [4, 18, 29, 39, 40, 45] in nuScenes is to transform and merge the Lidar points of non-annotated frames into its following annotated frame. This provides richer input information and enables a more reasonable velocity estimation. We follow this practice in all our experiments.



**Metrics.** We follow the official evaluation metric of nuScenes dataset [4]. For 3D detection, the main metrics are mean Average Precision (mAP) [9] and nuScenes detection score (NDS). The mAP uses a bird-eye-view center distance  $< 0.5\text{m}, 1\text{m}, 2\text{m}, 4\text{m}$  instead of standard box-overlap. NDS is a weighted average of mAP and other attributes metrics including translation, scale, orientation, velocity, and other box attributes [4]. For 3D tracking, nuScenes uses AMOTA [32]:

$$\text{AMOTA} = \frac{1}{n-1} \sum_{r \in \{\frac{1}{n-1}, \frac{2}{n-1}, \dots, 1\}} \max(0, 1 - \frac{IDS_r + FP_r + FN_r - (1-r)P}{rP}),$$

where  $r$  is a recall threshold,  $IDS_r, FP_r, FN_r$  are the number of ID switches, false positives, and false negatives until the top scored detections reaching recall  $r$ , respectively.  $P$  is the total number of annotated objects in the dataset, and  $n = 40$ .

## 5.1 Implementation details

Our implementation is based on the open-sourced code of CBGS [45]<sup>1</sup>. We experiment with both VoxelNet [35, 44, 45] encoder (termed CenterPoint-Voxel) and PointPillars [18] encoder (termed CenterPoint-Pillar). The original open-sourced CBGS [45] implementation did not reproduce the performance of the paper, and we fixed a few bugs and applied some improvements in the code. Specifically, we apply flip-augmentation on both  $X$  and  $Y$  axes, and used a smaller regression weight  $\lambda_{reg}$  (0.25 vs. originally 1). Our baseline is 51.9 mAP with 62.2 NDS for VoxelNet (vs. 49.6 mAP with 60.2 NDS reported in CBGS paper [45]) and 45.5 mAP with 58.4 NDS for PointPillars (vs. 28.9 mAP with 44.9 NDS reported in PointPillars paper [4, 18]) on nuScenes validation.

**Input size.** Following the nuScenes evaluation guideline, we set the detection range to  $[-51.2\text{m}, 51.2\text{m}]$  for the  $X$  and  $Y$  axis, and  $[-5\text{m}, 3\text{m}]$  for  $Z$  axis. CenterPoint-Voxel use a  $(0.1\text{m}, 0.1\text{m}, 0.2\text{m})$  voxel size, resulting in a  $1024 \times 1024 \times 40$  input voxel size. Our backbone uses a stride of 8, making the output resolution to be  $128 \times 128$ . We limit the maximum number of voxels to  $60k$  for sparse-convolution, following CBGS [45]. CenterPoint-Pillars uses a grid size of  $(0.2\text{m}, 0.2\text{m})$  and backbone stride 4, resulting in a  $512 \times 512$  input resolution and  $128 \times 128$  output resolution. The maximum number of pillars is  $30k$ .

**Training.** During training, we use random flipping along both  $X$  and  $Y$  axis, global scaling with a random factor from  $[0.95, 1.05]$ , random global rotation between  $[-\pi/8, \pi/8]$ , and random global translation of  $-0.2$  to  $0.2$  meters. We also use the ground-truth sampling [35], which copies and pastes points inside an annotated box from one frame to another frame. And we adopt the class-balanced sampling and class-grouped heads of CBGS [45] to alleviate the class imbalance problem of the dataset. The class-grouped heads cluster objects into different groups using class labels, and the detection head only detects objects in its corresponding group. Following SECOND and CBGS [35, 45], we optimize the model using adamW [22] optimizer with one-cycle learning rate policy [13], with max learning rate  $1e-3$ , weight decay 0.01, and momentum 0.85 to 0.95. We train the models with batch size 16 for 20 epochs on 4 V100 GPUs. Training takes 20 hours for CenterPoint-Pillar, and 40 hours for CenterPoint-Voxel. All ablation experiments are conducted in this same setting unless specified.

**Testing.** At inference, we keep the top 500 predictions in each group after filtering proposals with confidence less than 0.1. We then use the Circular NMS with a class specific radius to remove redundant boxes. We keep a maximum of 83 objects in each group after the NMS. The inference times are measured on an Intel Core i7-8086K CPU, and Titan Xp GPU.

## 5.2 Main Results

**3D Detection** We first present our detection results on nuScenes test set via their server with hidden annotation. We submitted our best result with flip test of a single model: CenterNet-Voxel with input grid size  $0.075\text{m}^2$ . Table 1 shows our results. Our model outperforms the last-year challenge winner CBGS [45] with multi-scale inputs and multi-model ensemble by 7.5% mAP, and 4.0% NDS,

<sup>1</sup><https://github.com/poodarchu/Det3D>

Table 1: State-of-the-art comparisons for 3D detection on nuScenes test set. We show the NDS, mAP, and mAP for each class. Abbreviations: construction vehicle (CV), pedestrian (Ped), motorcycle (Motor), and traffic cone (TC).

Method	mAP	NDS	Car	Truck	Bus	Trailer	CV	Ped	Motor	Bicycle	TC	Barrier
PointPillars [18]	30.5	45.3	68.4	23.0	28.2	23.4	4.1	59.7	27.4	1.1	30.8	38.9
WYSIWYG [16]	35.0	41.9	79.1	30.4	46.6	40.1	7.1	65.0	18.2	0.1	28.8	34.7
3DSSD [39]	42.6	56.4	81.2	47.2	61.4	30.5	12.6	70.2	36.0	8.6	31.1	47.9
PMPNet [40]	45.4	53.1	79.7	33.6	47.1	43.1	18.1	76.5	40.7	7.9	58.8	48.8
PointPainting [29]	46.4	58.1	77.9	35.8	36.2	37.3	15.8	73.3	41.5	24.1	62.4	60.2
CBGS [45]	52.8	63.3	81.1	48.5	54.9	42.9	10.5	80.1	51.5	22.3	70.9	65.7
Ours	<b>60.3</b>	<b>67.3</b>	<b>85.2</b>	<b>53.5</b>	<b>63.6</b>	<b>56.0</b>	<b>20.0</b>	<b>84.6</b>	<b>59.5</b>	<b>30.7</b>	<b>78.4</b>	<b>71.1</b>

Table 2: State-of-the-art comparisons for 3D tracking on nuScenes test set. We show AMOTA, the number of false positives (FP), false negatives (FN), id switches (IDS), and per-category AMOTA.  $\uparrow$  is for higher better and  $\downarrow$  is for lower better.

Method	AMOTA $\uparrow$	FP $\downarrow$	FN $\downarrow$	IDS $\downarrow$	Bicycle $\uparrow$	Bus $\uparrow$	Car $\uparrow$	Motor $\uparrow$	Ped $\uparrow$	Trailer $\uparrow$	Truck $\uparrow$
AB3D [32]	15.1	<b>15088</b>	75730	9027	0	40.8	27.8	8.1	14.1	13.6	1.3
Chiu et al. [6]	55.0	17533	33216	950	25.5	64.1	71.9	48.1	74.5	49.5	51.3
Ours	<b>63.8</b>	18612	<b>22928</b>	<b>760</b>	<b>32.1</b>	<b>71.1</b>	<b>82.9</b>	<b>59.1</b>	<b>76.7</b>	<b>65.1</b>	<b>59.9</b>

while being much simpler and faster<sup>2</sup>. We display a consistent performance improvement over all categories, and show more significant improvements in small categories (+7.5 mAP for traffic cone), and extreme-aspect ratio categories (+8.4 mAP for bicycle and +9.5 mAP for construction vehicle).

**3D Tracking** Table 2 shows our tracking performance on nuScenes test set. We perform our velocity-based closest distance matching described in Section 4.1 on our detection results. The tracking algorithm outperforms the last challenge winner Chiu et al. [6] by 8.8 AMOTA. Notably, our tracking does not require a separate motion model (e.g., a heavy Kalman filter in Chiu et al. [6]), and runs in a negligible time (1ms) with detection.

Table 3: Ablation studies for 3D detection on nuScenes validation. We ablate each component of CenterPoint with VoxelNet [44, 45] and PointPillars [18] encoder. The first row of each block shows the original performance in the corresponding paper and the second rows are our re-implemented baselines with the same settings as our proposed method.

Encoder	Re-implement	CenterPoint	Circular NMS	DCN Head	Hi-res	Flip-test	mAP	NDS	Runtime
VoxelNet							49.6	60.2	-
	$\checkmark$						51.9	62.2	78ms
	$\checkmark$	$\checkmark$					55.6	64.0	76ms
	$\checkmark$	$\checkmark$	$\checkmark$				55.4	63.8	<b>69ms</b>
	$\checkmark$	$\checkmark$	$\checkmark$	$\checkmark$			55.4	63.4	76ms
	$\checkmark$	$\checkmark$	$\checkmark$	$\checkmark$	$\checkmark$		56.1	64.5	101ms
	$\checkmark$	$\checkmark$	$\checkmark$	$\checkmark$	$\checkmark$	$\checkmark$	56.5	65.0	118ms
	$\checkmark$	$\checkmark$	$\checkmark$	$\checkmark$	$\checkmark$	$\checkmark$	58.8	66.9	440ms
PointPillars							<b>59.1</b>	<b>67.1</b>	449ms
	$\checkmark$						28.9	44.9	-
	$\checkmark$	$\checkmark$					45.5	58.4	42ms
	$\checkmark$	$\checkmark$	$\checkmark$				48.3	59.1	41ms
	$\checkmark$	$\checkmark$	$\checkmark$	$\checkmark$			48.3	59.1	<b>33ms</b>
					$\checkmark$		<b>48.6</b>	<b>59.4</b>	41ms

<sup>2</sup>See the runtime comparison in the ablation study. We did not provide runtime comparison on test set because: 1) many models contain ensemble; 2) most models do not report runtime, and the available runtimes are measured on different hardware.

Table 4: Ablation studies for 3D tracking on nuScenes validation. We show combinations of different detectors and trackers. CenterPoint-\* are our detectors. Point is our proposed tracker. M-KF is short for Mahalanobis distance-based Kalman filter, as is used in the last challenge winner Chiu et al. [6].

Method	Detector	Tracker	AMOTA↑	FP↓	FN↓	IDS↓	Tracking time	Total time
Ours (a)	CenterPoint-Voxel	Point	62.6	15410	21804	822	1ms	70ms
Ours (b)	CenterPoint-Pillar	Point	54.2	14090	25102	694	1ms	<b>34ms</b>
Ours (c)	CenterPoint-Voxel/Hi-res/Flip	Point	<b>65.5</b>	13978	<b>19844</b>	668	1ms	441ms
Ours (d)	CBGS [45]	Point	59.8	<b>11605</b>	23648	<b>462</b>	1ms	>192ms
Ours (e)	CenterPoint-Voxel	M-KF	57.3	14482	27812	917	91ms	160ms
Chiu et al. [6]	CBGS [45]	M-KF	56.1	12140	28387	679	91ms	>282ms

Table 5: Design choice experiments on nuScenes validation. We tried different hyper-parameters on CenterPoint-Pillars. The gaussian radius, regression weight, and flip-augmentations in training are important and can not directly be translated from 2D detection.

r	mAP↑	NDS↑	$\lambda_{reg}$	mAP↑	NDS↑		mAP↑	NDS↑
1	47.5	58.5	1.0	45.5	58.0	X-flip	44.3	56.4
0.7	47.9	58.7	0.5	47.2	58.6	double flip	<b>48.1</b>	<b>59.1</b>
0.1	<b>48.1</b>	<b>59.1</b>	0.25	<b>48.1</b>	<b>59.1</b>			

(a) Design choices of different gaussian radius for heatmaps.

(b) Design choices of regression weight.

(c) Design choices of different flip augmentations in training.

### 5.3 Ablation studies

Next, we ablate our contribution on nuScenes validation. Table 3 shows the importance of each component of CenterPoint and Table 5 shows the necessary hyper-parameter changes from 2D to 3D. For 3D detection, choosing a smaller regression weight and using flip augmentation on both axis each matter 3-4mAP, and setting a larger Gaussian radius gives another 0.6mAP gain. Switching from the anchors to our center-based representation (first and second rows of each block in Table 3) gives 3.7 mAP and 2.8 mAP improvements for VoxelNet and PointPillars, respectively. This convincingly shows the advantage of using center representation for 3D detection.

Using Circular NMS speeds up both pipelines by  $\sim 7$ ms with minor performance drop. Deformable convolutional layers [7] in the head gives a +0.4 mAP improvement on PointPillars and high resolution VoxelNet, presumably due to its better modeling of rotation. And using a  $1.5\times$  higher resolution input (i.e., (0.075m, 0.075m, 0.2m) for CenterPoint-Voxel) further improves 1.1mAP for VoxelNet at a cost of  $1.5\times$  processing time. Finally, we apply double-flip augmentation and use IoU-NMS for the results we submitted to the test server. This yields our best results on nuScenes validation, with 59.1mAP and 67.1 NDS, which closely matches our test set performance.

**3D Tracking.** Table 4 shows the ablation experiments of 3D tracking. We decompose the evaluation into the detector and tracker to make the comparison strict. Given the same detected objects, using our simple velocity-based closest point distance matching outperforms the Kalman filter-based Mahalanobis distance matching by 3-5 AMOTA (Ours (a) vs. Ours (e) and Ours (d) vs. Chiu et al. [6]). There are two sources of improvements: 1) we model the object motion with a learned point velocity, rather than modeling 3D bounding box dynamic with a Kalman filter; 2) we match objects by center point-distance instead of by a Mahalanobis distance of box states or 3D bounding box IoU. More importantly, our tracking is a simple for-loop for minimal distance searching without any hidden-state computation. This saves the computational overhead of a 3D Kalman filter [6] (91ms vs. 1ms).

Our tracker can trade off speed for accuracy using a heavier (Ours (c)) or lighter backbone (Ours (b)). Our tracker with PointPillars encoder runs end-to-end 3D detection and tracking in 30 FPS with 54.2 AMOTA and 59.1 NDS, and serves as a strong starting point for real-time 3D perception.



## 6 Conclusion

We proposed a center-based framework for simultaneous 3D object detection and tracking from the Lidar point cloud. Our method uses standard 3D point cloud encoder with a few convolutional layers in the head to produce a bird-eye-view heatmap and other dense regression outputs. Detection is a simple local peak extraction, and tracking is a closest-distance matching. CenterPoint is simple, real-time, and achieves state-of-the-art performance on nuScenes benchmark.

## References

- [1] Mayank Bansal, Alex Krizhevsky, and Abhijit Ogale. Chauffeurnet: Learning to drive by imitating the best and synthesizing the worst. *RSS*, 2019.
- [2] Philipp Bergmann, Tim Meinhardt, and Laura Leal-Taixe. Tracking without bells and whistles. *ICCV*, 2019.
- [3] Alex Bewley, Zongyuan Ge, Lionel Ott, Fabio Ramos, and Ben Upcroft. Simple online and realtime tracking. *ICIP*, 2016.
- [4] Holger Caesar, Varun Bankiti, Alex H. Lang, Sourabh Vora, Venice Erin Liong, Qiang Xu, Anush Krishnan, Yu Pan, Giancarlo Baldan, and Oscar Beijbom. nuscenes: A multimodal dataset for autonomous driving. *CVPR*, 2020.
- [5] Qi Chen, Lin Sun, Zhixin Wang, Kui Jia, and Alan Yuille. Object as hotspots: An anchor-free 3d object detection approach via firing of hotspots. *arXiv:1912.12791*, 2019.
- [6] Hsu-kuang Chiu, Antonio Prioletti, Jie Li, and Jeannette Bohg. Probabilistic 3d multi-object tracking for autonomous driving. *arXiv:2001.05673*, 2020.
- [7] Jifeng Dai, Haozhi Qi, Yuwen Xiong, Yi Li, Guodong Zhang, Han Hu, and Yichen Wei. Deformable convolutional networks. *ICCV*, 2017.
- [8] Martin Engelcke, Dushyant Rao, Dominic Zeng Wang, Chi Hay Tong, and Ingmar Posner. Vote3deep: Fast object detection in 3d point clouds using efficient convolutional neural networks. *ICRA*, 2017.
- [9] Mark Everingham, Luc Van Gool, Christopher KI Williams, John Winn, and Andrew Zisserman. The pascal visual object classes (voc) challenge. *IJCV*, 2010.
- [10] Ross Girshick. Fast r-cnn. *ICCV*, 2015.
- [11] Ross Girshick, Jeff Donahue, Trevor Darrell, and Jitendra Malik. Rich feature hierarchies for accurate object detection and semantic segmentation. *CVPR*, 2014.
- [12] Benjamin Graham, Martin Engelcke, and Laurens van der Maaten. 3d semantic segmentation with submanifold sparse convolutional networks. *CVPR*, 2018.
- [13] Sylvain Gugger. The 1cycle policy. <https://sgugger.github.io/the-1cycle-policy.html>, 2018.
- [14] Chenhang He, Hui Zeng, Jianqiang Huang, Xian-Sheng Hua, and Lei Zhang. Structure aware single-stage 3d object detection from point cloud. *CVPR*, 2020.
- [15] Kaiming He, Georgia Gkioxari, Piotr Dollár, and Ross Girshick. Mask r-cnn. *ICCV*, 2017.
- [16] Peiyun Hu, Jason Ziglar, David Held, and Deva Ramanan. What you see is what you get: Exploiting visibility for 3d object detection. *CVPR*, 2020.
- [17] H. Karunasekera, H. Wang, and H. Zhang. Multiple object tracking with attention to appearance, structure, motion and size. *IEEE Access*, 2019.
- [18] Alex H. Lang, Sourabh Vora, Holger Caesar, Lubing Zhou, Jiong Yang, and Oscar Beijbom. Pointpillars: Fast encoders for object detection from point clouds. *CVPR*, 2019.
- [19] Hei Law and Jia Deng. Cornernet: Detecting objects as paired keypoints. *ECCV*, 2018.
- [20] Tsung-Yi Lin, Priya Goyal, Ross Girshick, Kaiming He, and Piotr Dollar. Focal loss for dense object detection. *ICCV*, 2017.
- [21] Wei Liu, Dragomir Anguelov, Dumitru Erhan, Christian Szegedy, Scott Reed, Cheng-Yang Fu, and Alexander C Berg. Ssd: Single shot multibox detector. *ECCV*, 2016.

- [22] Ilya Loshchilov and Frank Hutter. Decoupled weight decay regularization. *ICLR*, 2019.
- [23] Charles R. Qi, Or Litany, Kaiming He, and Leonidas Guibas. Deep hough voting for 3d object detection in point clouds. *ICCV*, 2019.
- [24] Charles R Qi, Hao Su, Kaichun Mo, and Leonidas J Guibas. Pointnet: Deep learning on point sets for 3d classification and segmentation. *CVPR*, 2017.
- [25] Joseph Redmon and Ali Farhadi. Yolo9000: better, faster, stronger. *CVPR*, 2017.
- [26] Shaoqing Ren, Kaiming He, Ross Girshick, and Jian Sun. Faster r-cnn: Towards real-time object detection with region proposal networks. *NIPS*, 2015.
- [27] Shaoshuai Shi, Xiaogang Wang, and Hongsheng Li. Pointrcnn: 3d object proposal generation and detection from point cloud. *CVPR*, 2019.
- [28] Martin Simony, Stefan Milzy, Karl Amendey, and Horst-Michael Gross. Complex-yolo: An euler-region-proposal for real-time 3d object detection on point clouds. *ECCV*, 2018.
- [29] Sourabh Vora, Alex H Lang, Bassam Helou, and Oscar Beijbom. Pointpainting: Sequential fusion for 3d object detection. *CVPR*, 2020.
- [30] Dequan Wang, Coline Devin, Qi-Zhi Cai, Philipp Krähenbühl, and Trevor Darrell. Monocular plan view networks for autonomous driving. *IROS*, 2019.
- [31] Dominic Zeng Wang and Ingmar Posner. Voting for voting in online point cloud object detection. *RSS*, 2015.
- [32] Xinshuo Weng and Kris Kitani. A Baseline for 3D Multi-Object Tracking. *arXiv preprint arXiv:1907.03961*, 2019.
- [33] Nicolai Wojke, Alex Bewley, and Dietrich Paulus. Simple online and realtime tracking with a deep association metric. *ICIP*, 2017.
- [34] Kelvin Wong, Shenlong Wang, Mengye Ren, Ming Liang, and Raquel Urtasun. Identifying unknown instances for autonomous driving. *CORL*, 2019.
- [35] Yan Yan, Yuxing Mao, and Bo Li. Second: Sparsely embedded convolutional detection. *Sensors*, 2018.
- [36] Bin Yang, Wenjie Luo, and Raquel Urtasun. Pixor: Real-time 3d object detection from point clouds. *CVPR*, 2018.
- [37] Xue Yang, Qingqing Liu, Junchi Yan, Ang Li, Zhiqiang Zhang, and Gang Yu. R3det: Refined single-stage detector with feature refinement for rotating object. *arXiv:1908.05612*, 2019.
- [38] Xue Yang, Jirui Yang, Junchi Yan, Yue Zhang, Tengfei Zhang, Zhi Guo, Xian Sun, and Kun Fu. Scrddet: Towards more robust detection for small, cluttered and rotated objects. *ICCV*, 2019.
- [39] Zetong Yang, Yanan Sun, Shu Liu, and Jiaya Jia. 3dssd: Point-based 3d single stage object detector. *CVPR*, 2020.
- [40] Junbo Yin, Jianbing Shen, Chenye Guan, Dingfu Zhou, and Ruigang Yang. Lidar-based online 3d video object detection with graph-based message passing and spatiotemporal transformer attention. *CVPR*, 2020.
- [41] Xingyi Zhou, Vladlen Koltun, and Philipp Krähenbühl. Tracking objects as points. *arXiv:2004.01177*, 2020.
- [42] Xingyi Zhou, Dequan Wang, and Philipp Krähenbühl. Objects as points. In *arXiv:1904.07850*, 2019.
- [43] Yin Zhou, Pei Sun, Yu Zhang, Dragomir Anguelov, Jiyang Gao, Tom Ouyang, James Guo, Jiquan Ngiam, and Vijay Vasudevan. End-to-end multi-view fusion for 3d object detection in lidar point clouds. *CORL*, 2019.
- [44] Yin Zhou and Oncel Tuzel. Voxelnet: End-to-end learning for point cloud based 3d object detection. *CVPR*, 2018.
- [45] Benjin Zhu, Zhengkai Jiang, Xiangxin Zhou, Zeming Li, and Gang Yu. Class-balanced grouping and sampling for point cloud 3d object detection. *arXiv:1908.09492*, 2019.

## Appendix: Tracking algorithm

---

### Algorithm 1: Center-based Tracking

---

**Input :**  $T^{(t-1)} = \{(\mathbf{p}, \mathbf{v}, c, \mathbf{q}, id, a)_j^{(t-1)}\}_{j=1}^M$ : Tracked objects in the previous frame, with center  $\mathbf{p}$ , ground plane velocity  $\mathbf{v}$ , category label  $c$ , other bounding box attributes  $\mathbf{q}$ , tracking id  $id$ , and inactive age  $a$  (active tracks will have  $a = 0$ ).

$\hat{D}^{(t)} = \{(\hat{\mathbf{p}}, \hat{\mathbf{v}}, \hat{c}, \hat{\mathbf{q}})_i^{(t)}\}_{i=1}^N$ : Detections in the current frame in descending confidence.

**Output :**  $T^{(t)} = \{(\mathbf{p}, \mathbf{v}, c, \mathbf{q}, id, a)_j^K\}_{j=1}^K$ : Tracked Objects.

- 1 **Hyper parameters:** Matching distance threshold  $\tau$ ; Max inactive age  $A$ .
- 2 **Initialization:** Tracks  $T^{(t)}$ , and matches  $\mathcal{S}$  are initialized as empty sets.
- 3  $T^{(t)} \leftarrow \emptyset$
- 4  $\mathcal{S} \leftarrow \emptyset$  // Set of matched tracks
- 5  $F \leftarrow Cost(\hat{D}^{(t)}, T^{(t-1)})$  //  $F_{ij} = \|\hat{\mathbf{p}}_i^{(t)} - \hat{\mathbf{v}}, \mathbf{p}_j^{(t-1)}\|_2$
- 6 **for**  $i \leftarrow 1$  **to**  $N$  **do**
- 7      $j \leftarrow \arg \min_{j \notin \mathcal{S}} F_{ij}$
- 8     // Class-wise distance threshold  $\tau_c$
- 9     **if**  $F_{ij} \leq \tau_c$  **then**
- 10         // Associate with tracked object
- 11          $a_i^{(t)} \leftarrow 0$
- 12          $T^{(t)} \leftarrow T^{(t)} \cup \{(\hat{D}_i^{(t)}, id_j^{(t-1)}, a_i^{(t)})\}$
- 13          $\mathcal{S} \leftarrow \mathcal{S} \cup \{j\}$  // Mark track  $j$  as matched
- 14     **end**
- 15     **else**
- 16         // Initialize a new track
- 17          $a_i^{(t)} \leftarrow 0$
- 18          $T^{(t)} \leftarrow T^{(t)} \cup \{(\hat{D}_i^{(t)}, newID, a_i^{(t)})\}$
- 19     **end**
- 20 **end**
- 21 **for**  $j \leftarrow 1$  **to**  $M$  **do**
- 22     **if**  $j \notin \mathcal{S}$  **then**
- 23         // Unmatched tracks
- 24         **if**  $T.a_j^{(t-1)} < A$  **then**
- 25              $T.a_j^{(t)} \leftarrow T.a_j^{(t-1)} + 1$
- 26              $T.p_j^{(t)} \leftarrow T.p_j^{(t-1)} + T.v_j^{(t-1)}$  // Update the center location
- 27              $T^{(t)} \leftarrow T^{(t)} \cup \{T_j^{(t-1)}\}$
- 28         **end**
- 29     **end**
- 30 **end**
- 31 **Return**  $T^{(t)}$

---